42. S. Eichkorn, S. Wilhelm, H. Aufmhoff, K.-H. Wohlfrom, F. Arnold, *Geophys. Res. Lett.* **29**, 43-1 (2002); published online 27 July 2002 (10.1029/2002GL015044).
43. K.-H. Wohlfrom, S. Eichkorn, F. Arnold, P. Schulte, *Geophys. Res. Lett.* **27**, 3853 (2000).
44. F. Yu, R. P. Turco, *Geophys. Res. Lett.* **27**, 883 (2000).
45. C. D. O'Dowd *et al.*, *Geophys. Res. Lett.* **26**, 1707 (1999).
46. J. M. Makela *et al.*, *Geophys. Res. Lett.* **24**, 1219 (1997).
47. The depth of the space-charge layer depends on the transport of ions into and out of the layer by the drift current and by turbulent mixing, and may be shallower or deeper than 200 m (*55*).
48. R. Reiter, *Phenomena in Atmospheric and Environmental Electricity* (Elsevier, Amsterdam, 1992).
49. B. A Tinsley, R. A. Heelis, *J. Geophys. Res.* **98**, 10375 (1993).
50. B. A. Tinsley, *Space Sci. Rev.* **94**, 231 (2000).
51. S. N. Tripathi, R. G. Harrison, *Atmos. Res.* **62**, 57 (2002).
52. B. A. Tinsley, R. P. Rohrbaugh, M. Hei, K. V. Beard, *J. Atmos. Sci.* **57**, 2118 (2000).
53. R. Markson, *Nature* **291**, 304 (1981).
54. R. G. Harrison, *Geophys. Res. Lett.*, in press; published online 16 July 2002 (10.1029/2002GL014878).
55. R. Reiter, *Phenomena in Atmospheric and Environmental Electricity* (Elsevier, Amsterdam, 1992).
56. M. Lockwood, *J. Geophys. Res.*, in press (10.1029/2002JA009431).
57. We thank M. Lockwood for drawing Fig. 2. This work was facilitated in part by the Philip Leverhulme Prize (to K.S.C.), for which we are grateful to the Leverhulme Trust.

REVIEW GEOPHYSICS

The Spectral-Element Method, Beowulf Computing, and Global Seismology

Dimitri Komatitsch,* Jeroen Ritsema, Jeroen Tromp

The propagation of seismic waves through Earth can now be modeled accurately with the recently developed spectral-element method. This method takes into account heterogeneity in Earth models, such as three-dimensional variations of seismic wave velocity, density, and crustal thickness. The method is implemented on relatively inexpensive clusters of personal computers, so-called Beowulf machines. This combination of hardware and software enables us to simulate broadband seismograms without intrinsic restrictions on the level of heterogeneity or the frequency content.

There has been tremendous growth in the acquisition of seismic data as a result of the deployment of digital broadband networks over the past two decades. This wealth of data has led to the construction of improved models of velocity heterogeneity, anisotropy, and attenuation in Earth. These models have provided important constraints on Earth's composition and physical processes (*1*–*3*). Nevertheless, improvements in seismic models will require the development, implementation, and application of methods that accurately incorporate the effects of mantle and crustal velocity and density heterogeneity on seismic wave propagation.

For one-dimensional (1D) Earth models that vary as a function of depth only, such as the Preliminary Reference Earth Model (PREM) (*4*) (Fig. 1A), semi-analytical techniques are widely used to calculate seismograms. Two popular methods are normal-mode summation (*5*), in which one sums spherical eigenfunctions, and the reflectivity method (*6*), in which the solution for a layered model is expressed as a sum in the frequency–wave number domain. To compute seismograms in three-dimensional (3D) Earth models, such as shear-velocity mod-

Seismological Laboratory, California Institute of Technology, 1200 East California Boulevard, Pasadena, CA 91125, USA.

*To whom correspondence should be addressed; E-mail: komatits@gps.caltech.edu

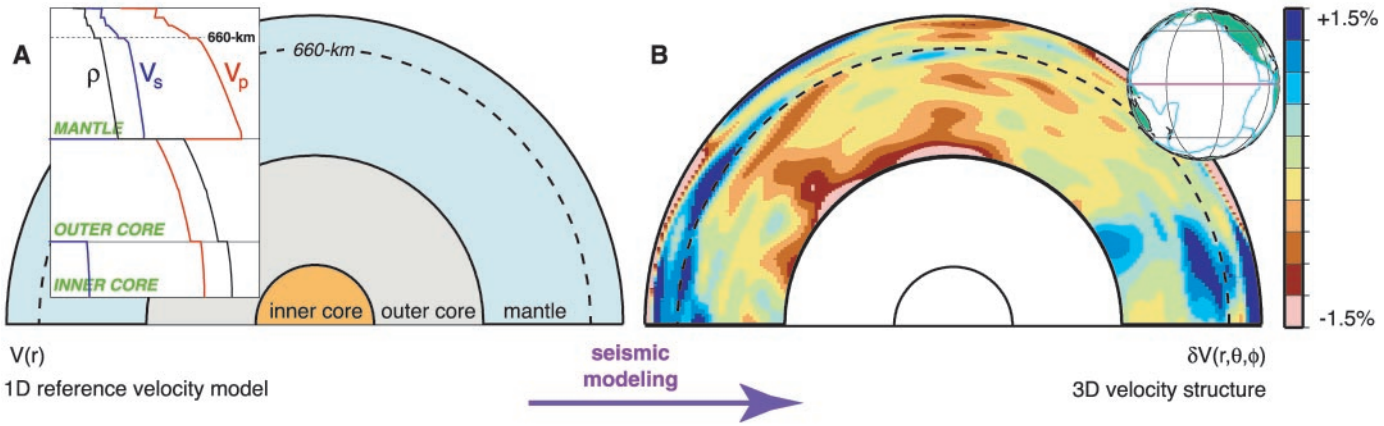

Fig. 1. Illustration of how seismic modeling is commonly conducted. (**A**) Cross section of Earth with the mantle, outer core, and inner core shaded blue, gray, and yellow, respectively. Superimposed on the left are 1D profiles of density ρ (black), shear velocity V_s (blue), and compressional velocity V_ρ (red) for PREM (*4*). The shear velocity is zero in the liquid outer core. Density and velocity vary smoothly throughout the model, except at compositional boundaries (e.g., the core-mantle boundary) or phase transitions in the upper mantle (e.g., at depths of 410 and 660 km). For 1D models such as PREM, which vary only as a function of depth, seismograms are computed using semi-analytical techniques such as normal-mode summation (*5*) or the reflectivity method (*6*). (**B**) Equatorial cross section through the Pacific mantle of shear velocity model S20RTS (*7*). Shown are relative lateral variations in shear velocity $\delta v(r,\theta,\phi)/v(r)$, where r denotes the radius; θ, colatitude; and ϕ, longitude. These 3D variations are superimposed on the velocity $v(r)$ in the 1D reference model. Red colors denote lower than average velocity perturbations, and blue colors denote higher than average perturbations. For 3D models, seismologists commonly use asymptotic methods such as ray theory (*8*) or the path-average approximation (*9*) to construct seismograms.

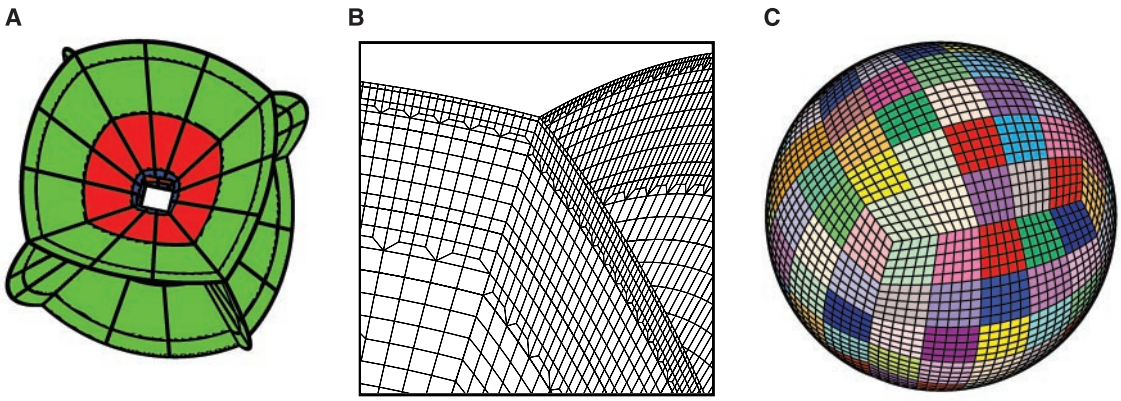

Fig. 2. (**A**) Illustration of the six blocks that constitute the "cubed sphere" (*31*). The crust and the mantle, outer core, and inner core are colored green, red, and blue, respectively. For clarity, the small cube at the center of Earth, which eliminates a mesh singularity (*27*), has been removed. (**B**) Close-up of the mesh at a corner between three blocks. The mesh size is doubled once below the crust, again below the 660-km discontinuity, and again just above the inner-core boundary. These three mesh doublings ensure a relatively constant number of grid points per wavelength and reduce the computational cost. Each of the six blocks contains 240 by 240 elements at the free surface and 30 by 30 elements at the inner-core boundary as a result of the doublings. (**C**) Global view of the mesh at the surface, illustrating that each of the six sides of the cubed sphere is divided into 25 slices, shown here with different colors, for a total of 150 slices. Each of the required 150 processors is responsible for computation of the wave field in one of these slices. In (C), the density of the surface mesh has been reduced by a factor of 5 in both lateral directions relative to the real mesh shown in (B) for clarity.

el S20RTS (*7*) (Fig. 1B), seismologists frequently resort to asymptotic techniques, in which one uses reasonable approximations to reduce the cost of the calculations. Three such approaches are ray theory (*8*), the path-average approximation (*9*), and nonlinear asymptotic coupling theory (*10*).

All tomographic inversions for 3D models of the mantle (the process by which one improves a given model on the basis of the difference between the observed and predicted seismograms) are rooted in perturbation theory. In travel-time tomography, the difference δT between the observed arrival time of a body wave and a prediction based on a 1D model is related to 3D perturbations in wave velocity, δv, through Fermat's principle

$$\delta T = -\int_{\text{ray path}} \frac{\delta v}{v^2}\, ds \qquad (1)$$

Here, v denotes either compressional velocity α or shear velocity β in the 1D reference model, and the integration is along the unperturbed ray path in the same model. Surface wave tomography involves an inversion of the difference between the observed and predicted phase, $\delta\Psi$, for lateral variations in Love or Rayleigh phase velocity, δc

$$\delta\Psi = -\omega\int_{\text{great circle}} \frac{\delta c}{c^2}\, ds \qquad (2)$$

In this case, the integration is along the great circle between a given epicenter and station, c denotes the phase velocity in the 1D reference model, and ω denotes the angular frequency. In normal-mode seismology, the difference between the observed and predicted mode eigenfrequency, $\delta\omega$, may be related to 3D variations in compressional velocity $\delta\alpha$, shear velocity $\delta\beta$, and density $\delta\rho$, through Rayleigh's principle

$$\delta\omega = \int_V (\delta\alpha K_\alpha + \delta\beta K_\beta + \delta\rho K_\rho)\, d^3\mathbf{r} \qquad (3)$$

The integration is over the entire volume V of Earth, and the sensitivity kernels K_α, K_β, and K_ρ are calculated on the basis of the modes and model parameters of the 1D reference model.

These three popular approximations define simple linear inverse problems. Howev-

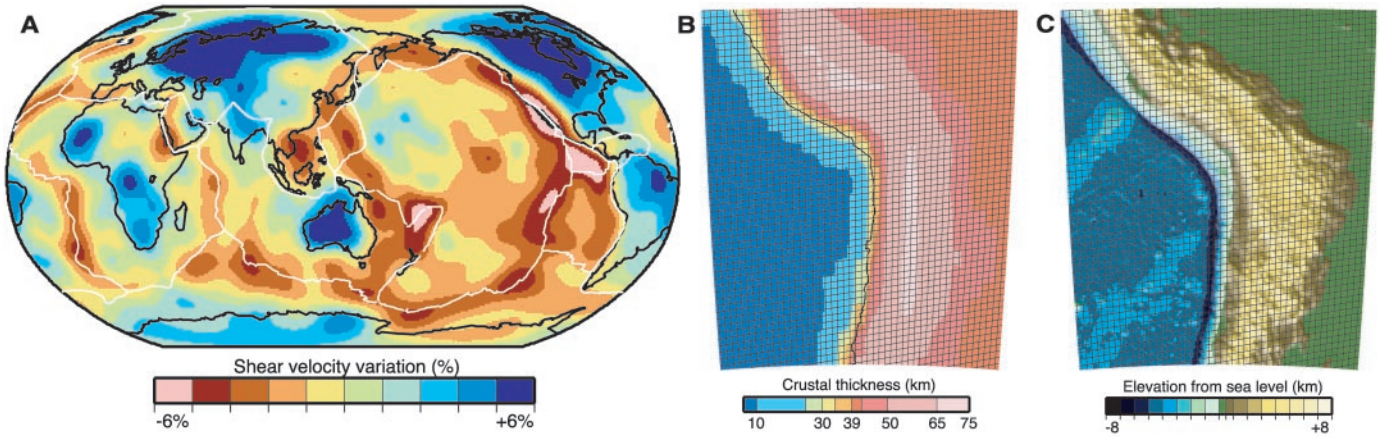

Fig. 3. Maps of models used in the SEM simulations. (**A**) Mantle shear velocity model S20RTS (*7*) at 120 km depth. Red colors denote slower than average shear-wave velocities, and blue colors denote higher than average velocities. (**B**) Close-up of crustal model CRUST2.0 (*34*) over a portion of western South America. The model provides a layered global crustal structure in 2° by 2° blocks. Red represents thicker than average crust, and blue represents thinner than average crust. (**C**) Topography and bathymetry model ETOPO5. The grid of surface elements is also shown in (B) and (C). In each spectral element we use a polynomial degree $N = 4$ (*28*, *29*). Therefore, each surface mesh element contains $(N + 1)^2 = 25$ grid points, which translates into an average grid spacing of about 10 km at the surface. A high-resolution mesh reduces the amount of numerical dispersion and anisotropy and thus is crucial for accurate results.

er, they may be of limited validity when we wish to recover velocity variations on length scales smaller than approximately 1000 km (*11*, *12*), close to the resolution provided by the most recent 3D models. To assess the quality of a 3D model, i.e., to evaluate the misfit between the data and the synthetic seismograms, the same approximate methods that were used to construct the model are employed. This means that there is a real risk that errors in the theory are mapped back into the model.

To overcome this dilemma, seismologists have begun to use numerical methods. Unfortunately, most of the current techniques come with severe restrictions, and they are frequently limited to two-dimensional (2D) axi-symmetric models to reduce the computational burden. Because of its simplicity and ease of implementation, the finite-difference technique has been introduced to simulate global seismic wave propagation (*13*, *14*). In this differential or "strong" formulation of the wave equation, displacement derivatives are approximated using differences between adjacent grid points, which makes the implementation of accurate boundary conditions difficult. The pseudospectral technique, in which the wave field is expanded in global basis functions (typically sines, cosines, or Chebyshev polynomials) (*15*, *16*), has similar limitations because it is also based on a strong formulation. Nevertheless, this method has been used to simulate wave propagation in a portion of the mantle (*17*). For both finite-difference and pseudospectral techniques, gridding the entire globe remains an outstanding challenge (*18*). Alternative approaches, such as the direct-solution method (*19*, *20*) and the coupled-mode method (*21*, *22*), which are based on an integral or "weak" formulation of the equation of motion, are numerically expensive because of the wide coupling bandwidth required in the presence of strong lateral heterogeneities. Also, handling variations in crustal thickness is difficult because effects due to boundary undulations are linearized. Because direct-solution and coupled-mode methods involve the manipulation of large matrices, they are restricted to modeling long-period seismograms (typically periods greater than 80 s).

To be practical, a method for the simulation of global seismic wave propagation should accurately incorporate effects due to velocity and density heterogeneity, anisotropy, anelasticity, sharp velocity and density contrasts, crustal thickness variations, topography, ellipticity, rotation, self-gravitation, and the oceans without intrinsic restrictions on the level of heterogeneity or the applicable frequency range (*23*). The spectral-element method (SEM) is such a method.

The Method

The SEM was developed more than 15 years ago in computational fluid dynamics (*24*). It combines the flexibility of the finite-element method with the accuracy of the pseudospectral method. In a classical finite-element method, the points that are used to define the geometry of an element are also used for the interpolation of the wave field. In a SEM, the wave field is expressed in terms of higher-degree Lagrange polynomials on Gauss-Lobatto-Legendre interpolation points. This ensures minimal numerical grid dispersion and anisotropy. The most important property of the SEM is that the mass matrix is exactly diagonal by construction, which drastically simplifies the implementation and reduces the computational cost because one can use an explicit time integration scheme without having to invert a linear system. The SEM was first introduced in local and regional seismology in the 1990s (*25*, *26*) and only recently in global seismology (*27*–*29*). When part of the model is 1D, the method can be coupled with a normal-mode solution in the spherically symmetric region to reduce the numerical cost and to facilitate the analysis of higher frequency signals (*30*).

The spectral-element mesh for Earth is based on the so-called "quasi-uniform gnomonic projection" or "cubed-sphere" (*31*), which is an analytical mapping from the cube to the sphere (Fig. 2). The mesh honors the first- and second-order discontinuities in model PREM (*4*) and accommodates crustal thickness variations, surface topography, and ellipticity. A small cube at Earth's center matches perfectly with the cubed-sphere mesh for the surrounding globe, thereby eliminating a mesh singularity (*27*).

For calculations on a parallel computer, the six building blocks that constitute the

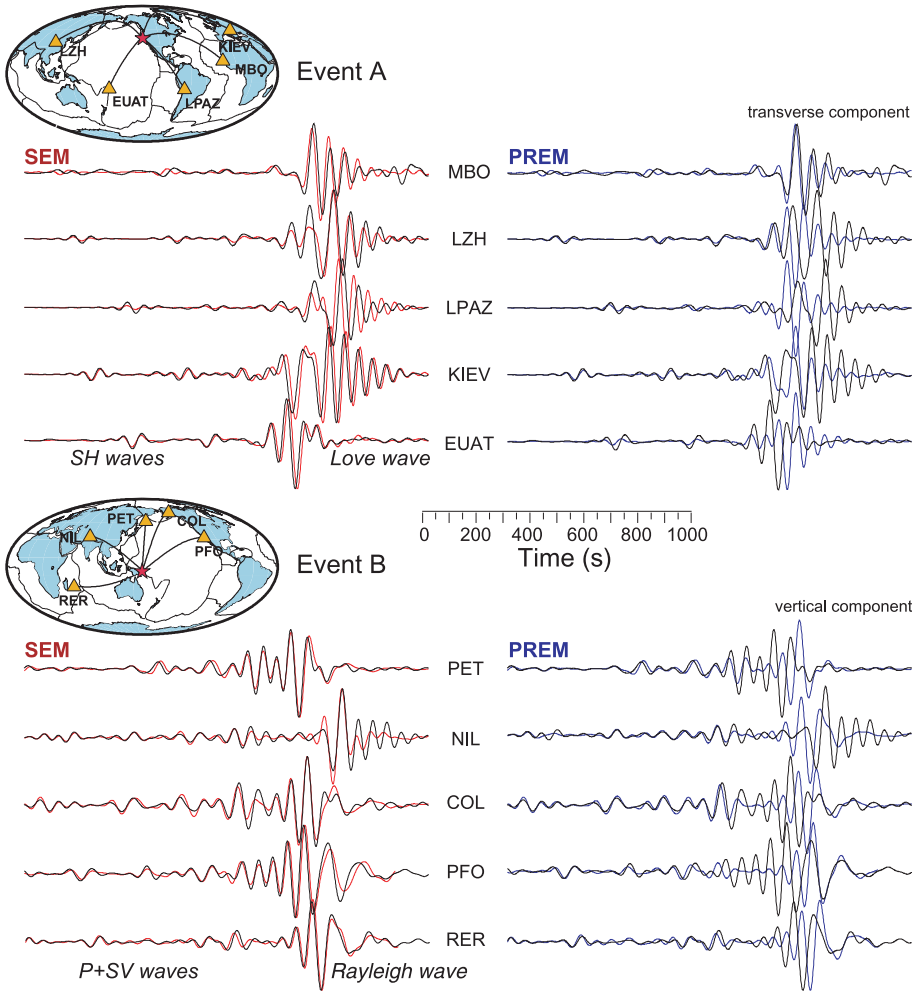

Fig. 4. Lowpass filtered (period > 50 s) recordings of (**top**) the 19 February 1995 off-shore California earthquake (M_w 6.6, event A) at stations MBO (Senegal), LZH (China), LPAZ (Bolivia), KIEV (Ukraine), and EUAT (Tonga) and (**bottom**) the 14 August 1995, New Britain earthquake (M_w 6.7, event B) at stations PET (Russia), NIL (Pakistan), COL (Alaska), PFO (California), and RER (La Réunion island). Superimposed on the recordings (black) are 1D PREM synthetic seismograms (blue) and fully 3D SEM synthetic seismograms (red). The maps plotted above the seismograms indicate station locations (orange triangles), earthquake epicenters (red stars), and great-circle paths between epicenters and stations. Plate boundaries are drawn with thin black lines.

cubed sphere are each divided into 25 slices, such that 150 processors are used in a simulation (Fig. 2). Each processor is responsible for propagating waves in one of the slices, thus distributing and balancing the load evenly. After each time step, the results of the calculations on the edges of the slices are communicated to neighboring slices through a 100 megabits/s Ethernet network using the Message-Passing Interface (MPI) (*32*).

In the crust and mantle, we solve the weak form of the wave equation (*28*)

$$\int_M \rho\, \mathbf{w} \cdot \partial_t^2 \mathbf{s}\, d^3\mathbf{r} = -\int_M \nabla \mathbf{w} : \mathbf{T}\, d^3\mathbf{r} + \mathbf{M} : \nabla w - \int_{CMB} \partial_t \chi\, \mathbf{w} \cdot \hat{\mathbf{n}}\, d^2\mathbf{r} \quad (4)$$

where **s** denotes the displacement vector; **T**, the stress tensor; ρ, density; **w**, any test vector; **M**, the source moment tensor; M, the mantle and crust; CMB, the core-mantle boundary; $\hat{\mathbf{n}}$ the unit outward normal on that boundary; and χ, the fluid potential at the top of the outer core. In the SEM, stress may be related to strain by the full, anisotropic elastic tensor on the basis of Hooke's law, and attenuation is accommodated by the introduction of memory variables (*28*).

The use of a potential in the fluid provides a natural way of coupling the solid and fluid regions and reduces the computational burden because only one scalar variable is needed. In the fluid outer core, we solve the weak form of the acoustic wave equation for the scalar potential χ

$$\int_{OC} \kappa^{-1} w \partial_t^2 \chi\, d^3\mathbf{r} = -\int_{OC} \rho^{-1} \nabla w \cdot \nabla \chi\, d^3\mathbf{r} + \int_{CMB} w \hat{\mathbf{n}} \cdot \partial_t \mathbf{s}\, d^2\mathbf{r} - \int_{ICB} w \hat{\mathbf{n}} \cdot \partial_t \mathbf{s}\, d^2\mathbf{r} \quad (5)$$

where κ denotes the adiabatic bulk modulus; *w*, any scalar test function; OC, the outer core; and ICB, the inner-core boundary. In the solid inner core, we solve the weak form

$$\int_{IC} \rho\, \mathbf{w} \cdot \partial_t^2 \mathbf{s}\, d^3\mathbf{r} = -\int_{IC} \nabla \mathbf{w} : \mathbf{T}\, d^3\mathbf{r} + \int_{ICB} \partial_t \chi\, \mathbf{w} \cdot \hat{\mathbf{n}}\, d^2\mathbf{r} \quad (6)$$

where IC denotes the inner core. The traction-free boundary condition at Earth's free surface is satisfied automatically by this weak form of the equations because of the integration by parts over the volume of Earth (*28*). Complications associated with the oceans, rotation, and self-gravitation may be accommodated by solving a similar system of weak equations with additional terms (*29*).

Contrary to numerical techniques based on the strong form of the equation of motion, the SEM facilitates the accurate simulation of diffracted body and surface waves, including their large physical dispersion. This is important because, as the largest signals in seismograms, surface waves are used routinely in seismology for velocity model building and earthquake rupture analysis, and diffracted body waves are pivotal in studies of the core-mantle boundary region.

We have implemented the SEM for global wave propagation on a cluster of personal computers (PCs), a so-called Beowulf machine with 150 processors and 75 gigabytes of memory. This parallel machine allows us to compute complete global seismograms that are accurate up to frequencies of 55 mHz, comparable to seismic signals used in waveform-based global tomography. It takes about 48 hours to compute seismograms with a duration of 60 min for a single earthquake (*33*).

Effects of 3D Heterogeneity

With the hardware available to us, it is currently only practical to explore wave propagation effects for a small number of models of the crust and mantle. Therefore, we limit ourselves to computing SEM seismograms for model S20RTS of the mantle (*7*), model CRUST2.0 of the crust (*34*), and topography and bathymetry model ETOPO5 (from the National Oceanic and Atmospheric Administration) (Fig. 3). These models represent the state-of-the-art in global seismology, and the SEM gives us an opportunity to assess their quality.

We compared recordings of the 19 February 1995 off-shore California earthquake (event A) and the 14 August 1995 New Britain earthquake (event B) with 1D PREM and fully 3D SEM synthetic seismograms (Fig. 4). This comparison illustrates typical effects of 3D heterogeneity on the waveforms of surface waves that propagate through the highly heterogeneous crust and uppermost mantle. The dispersion of Love and Rayleigh waves that have propagated through both continental and oceanic regions (e.g., event A at seismic station LZH in China and event B at NIL in Pakistan) is generally matched better by the 3D SEM synthetic seismograms than the 1D PREM synthetics. The most dramatic improvements in waveform fits are obtained for predominantly oceanic paths. Trans-Pacific Love (e.g., event A at EUAT in Tonga) and Rayleigh waves (e.g., event B at PFO in California) propagate nearly a minute faster than predicted by the PREM model because the oceanic crust is thinner (< 10 km) than the 21.4-km-thick globally averaged crust incorporated in PREM. Moreover, relative amplitudes of surface and body waves, which are to a large extent sensitive to near-source structure, are also in better agreement. A more extensive analysis based on simulations for more than 50 events revealed that models S20RTS and CRUST2.0 adequately explain body wave travel-time anomalies at periods greater than 18 s but that, in most cases, surface wave dispersion is only accurate at periods greater than 40 s. This suggests that

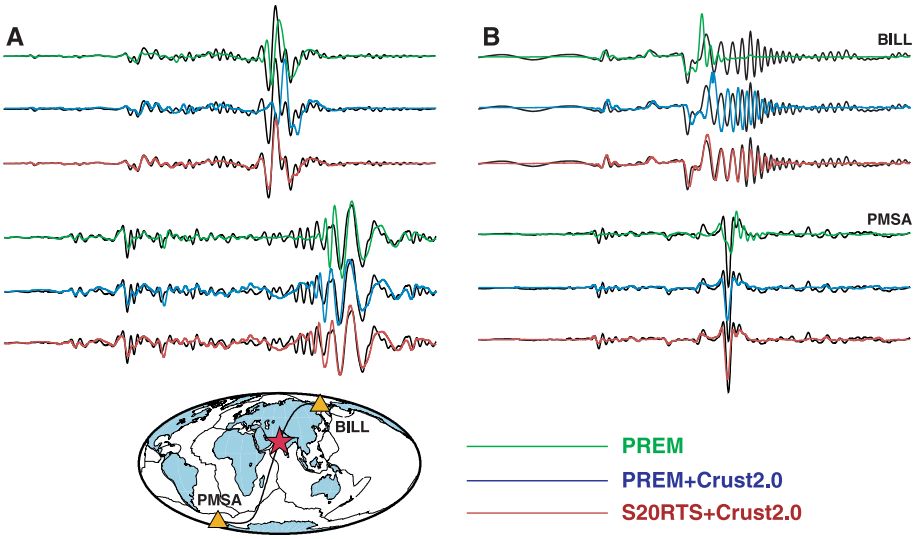

Fig. 5. Comparison of Rayleigh (**A**) and Love (**B**) wave recordings (black) for the 26 January 2001, Bhuj, India, earthquake (M_w 7.6) at stations BILL (Russia) and PMSA (Antarctica) for the PREM model (green), a model with the CRUST2.0 crustal structure overlying a PREM mantle (blue), and fully 3D synthetic seismograms (red) (CRUST2.0 combined with S20RTS). The figure illustrates the relative importance of 3D crustal and mantle structure. The map indicates station locations (orange triangles), the event location (red star), and great-circle paths between the epicenter and stations. (Courtesy V. Hjörleifsdóttir.)

the crustal model can still be substantially improved.

Even at relatively long periods, both the heterogeneous crust and mantle affect surface wave propagation (Fig. 5). For the 26 January 2001 Bhuj earthquake in India, we find that the oscillatory nature of the Love wave propagating through the relatively thick Eurasian crust (station BILL in Russia) and the impulsive nature of the Love wave propagating through oceanic crust (station PMSA in Antarctica) are generally well reproduced by synthetic seismograms for models that include a realistic crustal structure (e.g., CRUST2.0). However, an acceptable fit to surface wave phase is only attained when a good 3D model of the mantle (e.g., S20RTS) is invoked as well.

While most models of shear and compressional velocity variations are constrained by body wave travel-time and surface wave phase-delay data, seismic wave amplitudes provide important complementary constraints. To illustrate this point, we compared observed and predicted SS/S amplitude ratios (Fig. 6, A and B) (*35*). The maps have a correlation coefficient of 0.54, which means that they are correlated at the 95% confidence level. Because the 3D model adopts the attenuation, i.e., radial shear Q, structure of PREM, this implies that a large portion of the observed SS/S amplitude ratio is due to elastic focusing effects rather than attenuation. The SEM-predicted SS/S amplitude ratio is an underestimate of the actual elastic focusing effects because seismic amplitudes are determined by gradients and second derivatives of the velocity model, which are reduced by damping in the tomographic inversion.

Figure 6C shows the estimated distribution of $\delta \ln Q$ (*36*), and Fig. 6D shows differential t^* measurements (*37*), δt^*_{SS-S}, both of which are estimates of wave attenuation. The correlation coefficients between the observed and predicted SS/S amplitude ratio maps and the $\delta \ln Q$ map are 0.33 and 0.23, respectively. This suggests that the $\delta \ln Q$ map is the result of a tomographic inversion that has not fully accounted for elastic focusing effects. Because of incomplete global coverage in the differential t^* measurements, it is not possible to calculate a proper correlation between the observed SS/S amplitude ratio and the δt^*_{SS-S} measurements, but, in general, low values of δt^*_{SS-S}, indicative of low attenuation, correlate with observed SS/S amplitude ratios greater than one and high values of δt^*_{SS-S}, indicative of strong attenuation, correlate with SS/S ratios less than one. Again, this suggests that a large portion of the δt^*_{SS-S} signal reflects elastic focusing effects and not attenuation.

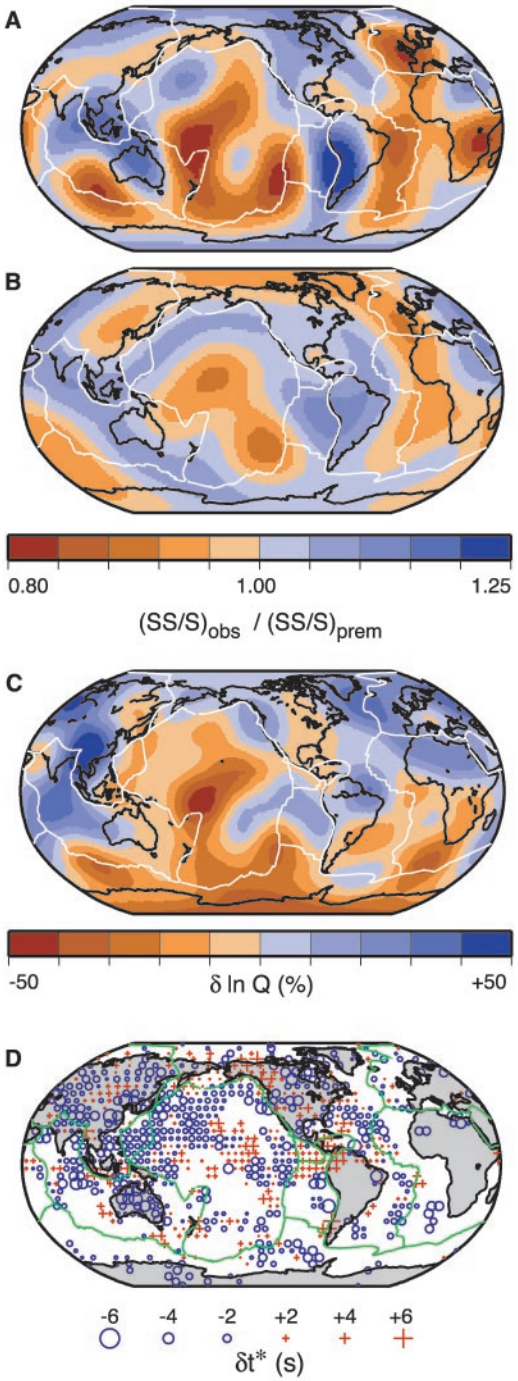

Fig. 6. Distribution of SS/S amplitude anomalies inferred from (**A**) long-period transverse component shear waveforms and (**B**) SEM synthetic seismograms. The values plotted at the SS surface reflection points have been expanded into spherical harmonics up to degree and order six (*35*). Blue colors denote SS/S amplitude ratios larger than predicted by PREM, and red colors denote SS/S amplitude ratios lower than predicted by PREM. (**C**) Lateral variations in $\delta \ln Q$ at 350-km depth from (*36*). Red colors denote stronger attenuation, and blue colors denote weaker attenuation. (**D**) Differential $\delta t^*_{SS-S} = \int_{SS\ ray} (\beta Q)^{-1}\, ds - \int_{S\ ray} (\beta Q)^{-1}\, ds$ distribution from (*37*). Large values of δt^*_{SS-S} are often interpreted in terms of strong attenuation, whereas small values reflect weak attenuation. The data have been smoothed by averaging at least three residuals with SS reflection points that fall within a circular cap with a radius of 5°.

Perspectives

From a theoretical and numerical point of view, there is no upper limit on the seismic frequency content that can be simulated with the SEM. The size of our current PC cluster restricts the simulation of seismic wave propagation to frequencies lower than 55 mHz. The "Earth Simulator" (35 teraflops) in Japan and the "ASCI-White" (7 teraflops) in the United States are today's fastest computers. On the basis of projected advances in computer technology, it is conceivable that computers as much as a factor of 100 faster (i.e., capable of 1 petaflop) will be available by the year 2010. Such computational power will make routine use of the SEM possible both in detailed forward modeling studies of anomalous broadband signals (*38*, *39*) and eventually in global tomography.

Classic seismological techniques will remain useful for many years to come because they provide an important baseline reference. Travel-time and amplitude anomalies will continue to be reported relative to this baseline. Similarly, asymptotic methods will continue to play an important role because they provide an inexpensive means for interrogating a 3D model. The SEM enables seismologists to calculate highly accurate seismograms that can be used to further improve 3D models. The calculation of synthetic seismograms for a given model is commonly referred to as the "forward" problem, whereas the construction of a model given a set of data is referred to as the "inverse" problem. Effectively, the SEM has solved the forward problem in long-period global seismology. On the basis of the aforementioned projected advances in computational power, addressing the inverse problem with the SEM will become feasible in the foreseeable future.

In some ways, the SEM is well ahead of current tomographic practice. Fully anisotropic models of the crust, mantle, and inner core can already be accommodated. The method also provides for models that exhibit lateral variations in both elastic and anelastic structure. As much as the establishment of global digital networks of seismometers revolutionized global seismology in the past two decades, we believe that the SEM offers unique opportunities for the development in the next decade of a new generation of high-quality mantle models and the determination of better earthquake source parameters (*40*).

References and Notes

1. J.-P. Montagner, *Pure Appl. Geophys.* **151**, 223 (1998).
2. B. Romanowicz, *Pure Appl. Geophys.* **153**, 257 (1998).
3. T. W. Becker, L. Boschi, *Geochem. Geophys. Geosyst.* **3** (2002).
4. A. M. Dziewonski, D. L. Anderson, *Phys. Earth Planet. Inter.* **25**, 297 (1981). PREM is a 1D transversely isotropic, anelastic velocity and density reference model of Earth.
5. F. Gilbert, *Geophys. J. R. Astron. Soc.* **22**, 223 (1970).
6. K. Fuchs, G. Muller, *Geophys. J. R. Astron. Soc.* **23**, 417 (1971).
7. J. Ritsema, H. J. Van Heijst, J. H. Woodhouse, *Science* **286**, 1925 (1999). Mantle model S20RTS is a degree 20 shear velocity model based on fundamental and higher-mode Rayleigh wave dispersion, teleseismic body wave travel times, and normal-mode splitting data. It is assumed that compressional velocity heterogeneity α is identical to shear velocity heterogeneity β in S20RTS, except for a depth-dependent scaling factor, $R = \delta\ln\beta/\delta\ln\alpha$, which increases linearly from 1.3 at the surface to 3.0 at the core-mantle boundary.
8. V. Červený, *Seismic Ray Theory* (Cambridge Univ. Press, Cambridge, 2001).
9. J. H. Woodhouse, A. M. Dziewonski, *J. Geophys. Res.* **89**, 5953 (1984).
10. X.-D. Li, T. Tanimoto, *Geophys. J. Int.* **112**, 92 (1993).
11. G. Nolet, F. A. Dahlen, *J. Geophys. Res.* **105**, 19,043 (2000).
12. J. Spetzler, J. Trampert, R. Snieder, *Geophys. Res. Lett.* **28**, 2341 (2001).
13. H. Igel, M. Weber, *Geophys. Res. Lett.* **23**, 415 (1996).
14. E. Chaljub, A. Tarantola, *Geophys. Res. Lett.* **24**, 2613 (1997).
15. T. Furumura, B. L. N. Kennett, M. Furumura, *Geophys. J. Int.* **135**, 845 (1998).
16. V. F. Cormier, *Geophys. J. Int.* **136**, 373 (1999).
17. H. Igel, *Geophys. J. Int.* **136**, 559 (1999).
18. The main difficulty comes from the singularity of coordinates at the center of Earth.
19. T. Hara, S. Tsuboi, R. Geller, *Geophys. J. Int.* **104**, 523 (1991).
20. R. J. Geller, T. Ohminato, *Geophys. J. Int.* **116**, 421 (1994).
21. J. Park, *J. Geophys. Res.* **91**, 6441 (1986).
22. P. Lognonné, B. Romanowicz, *Geophys. J. Int.* **102**, 365 (1990).
23. Not all of these effects play an important role at any given frequency: the effects of self-gravitation and rotation only matter at periods longer than about 100 s, whereas the effect of the oceans is only observed at periods less than about 50 s.
24. A. T. Patera, *J. Comput. Phys.* **54**, 468 (1984).
25. E. Priolo, J. M. Carcione, G. Seriani, *J. Acoust. Soc. Am.* **95**, 681 (1994).
26. D. Komatitsch, J. P. Vilotte, *Bull. Seismol. Soc. Am.* **88**, 368 (1998).
27. E. Chaljub, thesis, Université Paris VII Denis Diderot (2000). This thesis introduces the first implementation of the SEM for global wave propagation.
28. D. Komatitsch, J. Tromp, *Geophys. J. Int.* **149**, 390 (2002). The article discusses the theoretical and numerical aspects of the SEM and validates the method for seismic wave propagation at the scale of the entire globe.
29. D. Komatitsch, J. Tromp, *Geophys. J. Int.* **150**, 303 (2002).
30. Y. Capdeville, E. Chaljub, J. P. Vilotte, J. P. Montagner, *Geophys. J. Int.*, in press.
31. R. Sadourny, *Mon. Weather Rev.* **100**, 136 (1972).
32. W. Gropp, E. Lusk, N. Doss, A. Skjellum, *Parallel Comput.* **22**, 789 (1996).
33. The cost of the calculation is due to the fact that the mesh contains 498 million degrees of freedom.
34. C. Bassin, G. Laske, G. Masters, *EOS* **81**, F897 (2000). To avoid artificial reflections between block edges, we slightly smooth model CRUST2.0 by averaging over spherical caps with a 2° radius.
35. J. Ritsema, L. A. Rivera, D. Komatitsch, J. Tromp, H. J. van Heijst, *Geophys. Res. Lett.* **29**, 72 (2002). The observed SS/S amplitude ratio [the ratio of $(SS/S)_{observed}$ to $(SS/S)_{PREM}$] is determined by cross-correlating long-period (period $>$ 18 s) transverse component SS and S waveforms with normal-mode PREM synthetic seismograms on the basis of Harvard centroid moment tensor source parameters. The accuracy of the observed SS/S amplitude ratio is not affected by uncertainties in earthquake source parameters. The predicted SS/S amplitude ratio (the ratio of $(SS/S)_{SEM}$ to $(SS/S)_{PREM}$) is determined by applying the same cross-correlation method to SEM synthetic seismograms computed for 50 earthquakes at 400 worldwide stations, which renders a geographical distribution of SS bounce points that is similar to the data. This calculation required a total of 100 days of dedicated CPU time on our PC cluster.
36. B. Romanowicz, Y. C. Gung, *Science* **296**, 513 (2002).
37. F. J. L. Reid, J. H. Woodhouse, H. J. van Heijst, *Geophys. J. Int.* **145**, 615 (2001).
38. L. X. Wen, P. G. Silver, D. James, R. Kuehnel, *Earth Planet. Sci. Lett.* **189**, 141 (2001).
39. S. D. Ni, E. Tan, M. Gurnis, D. V. Helmberger, *Science* **296**, 1850 (2002).
40. We encourage interested research groups to download the SEM software package from the "Theoretical and Computational Seismology" Web page of the Seismological Laboratory at Caltech (www.gps.caltech.edu/~jtromp/research).
41. This is contribution no. 8886 of the Division of Geological and Planetary Sciences, California Institute of Technology. We thank B. Romanowicz for making her $\delta\ln Q$ map available, F. Reid for providing her δt^*_{SS-S} map, and two anonymous reviewers for helpful comments. This research was funded in part by the NSF.